Nanoscale Research Letters

NANO EXPRESS

Open Access

High-Hole-Mobility Metal–Organic Framework as Dopant-Free Hole Transport Layer for Perovskite Solar Cells

Ruonan Wang[1†], Weikang Yu[1,2†], Cheng Sun[1†], Kashi Chiranjeevulu[3], Shuguang Deng[4], Jiang Wu[5], Feng Yan[6], Changsi Peng[7], Yanhui Lou[1*], Gang Xu[3*] and Guifu Zou[1*]

Abstract

A dopant-free hole transport layer with high mobility and a low-temperature process is desired for optoelectronic devices. Here, we study a metal–organic framework material with high hole mobility and strong hole extraction capability as an ideal hole transport layer for perovskite solar cells. By utilizing lifting-up method, the thickness controllable floating film of Ni_3(2,3,6,7,10,11-hexaiminotriphenylene)$_2$ at the gas–liquid interface is transferred onto ITO-coated glass substrate. The Ni_3(2,3,6,7,10,11-hexaiminotriphenylene)$_2$ film demonstrates high compactness and uniformity. The root-mean-square roughness of the film is 5.5 nm. The ultraviolet photoelectron spectroscopy and the steady-state photoluminescence spectra exhibit the $Ni_3(HITP)_2$ film can effectively transfer holes from perovskite film to anode. The perovskite solar cells based on $Ni_3(HITP)_2$ as a dopant-free hole transport layer achieve a champion power conversion efficiency of 10.3%. This work broadens the application of metal–organic frameworks in the field of perovskite solar cells.

Keywords: Dopant-free hole transport materials, Metal–organic frameworks, Perovskite solar cells, High hole mobility, Ni_3(2,3,6,7,10,11-hexaiminotriphenylene)$_2$

Introduction

Organic–inorganic hybrid perovskite solar cells (PSCs) are drawing more and more attention due to its rapid upgrade of device efficiency [1–9]. So far, the highest certified power conversion efficiency (PCE) of the PSCs has reached up to 25.5% [10], approaching that of monocrystalline silicon-based solar cells. PSCs are thin-film devices, and the perovskite light active layer is sandwiched between anode and cathode. To improve the PCE and stability, the suitable hole transport layers (HTLs) are inserted between perovskite layers and anodes [11–15]. Usually, HTLs have been proven to be an important part of PSCs to reduce carrier recombination and collect holes effectively, thereby increasing open-circuit voltage and fill factor [16]. Ideal HTLs should incorporate the following desirable characteristics: (i) high carrier mobility to facilitate effective transportation holes. (ii) high stability to prolong device life. (iii) low-temperature solution process for deposition of the film.

The HTLs are divided into organic and inorganic materials. The organic HTLs have high-quality film and adjustable bandgap [17, 18]. The representative organic materials used in perovskite solar cells are poly(3,4-ethylenedioxythiophene):poly(styrene sulfonate) [19], poly[bis(4-phenyl)(2,4,6-trimethylphenyl)amine] [20],

*Correspondence: yhlou@suda.edu.cn; gxu@fjirsm.ac.cn; zouguifu@suda.edu.cn
†Ruonan Wang, Weikang Yu and Cheng Sun: These three authors contributed equally to the work
[1] College of Energy, Soochow Institute for Energy and Materials Innovations, and Key Laboratory of Advanced Carbon Materials and Wearable Energy Technologies of Jiangsu Province, Soochow University, Suzhou 215123, People's Republic of China
[3] State Key Laboratory of Structural Chemistry, Fujian Institute of Research on the Structure of Matter, Chinese Academy of Sciences, Fuzhou 350002, Fujian, China
Full list of author information is available at the end of the article

2,2′,7,7′-tetrakis(*N*,*N*′-di-*p*-methoxyphenylamine)-9,9′-spirobiflurorene (Spiro-OMeTAD) [21] and poly(3-hexylthiophene) [22–25]. However, the hole mobility of the most organic HTLs is within 10^{-2}–10^{-6} $cm^2 \cdot V^{-1} \cdot S^{-1}$ [26]. It limits the ability to transport holes from active layer to electrode and further restricts device efficiency. Doping is a useful method to enhance carriers mobility of organic semiconductors. For example, the hole mobility improves enormously after 4-*tert*-butyl-pyridine and bis (trifluoromethane) sulfonimide lithium salt are added into Spiro-OMeTAD. However, it also brings the problem of device instability due to the hygroscopicity of the additives, and so on [27, 28].

Traditional inorganic materials such as V_2O_5, Cu_2O, MoO_3, CuSCN, NiO_x, and their derivatives have been widely studied due to the advantages of excellent long-term stability and high intrinsic hole mobility [29–34]. Nevertheless, most of these materials are prepared through high annealing temperature, O_2 plasma, too time-consuming, or limited solubility. These drawbacks hinder their further development in large-scale applications and flexible devices. Therefore, it is necessary to find new HTLs with high mobility, low-temperature process, and high stability.

Metal–organic frameworks (MOFs) possess properties of high degree flexibility, including adjustable electrical [35], optical [35], and mechanical properties [36, 37]. It has attracted much attention in the fields of electronic devices [38, 39], such as memristors, field-effect transistors, supercapacitors [40], and various sensor architectures [41–43]. In recent years, MOFs have been applied in PSCs due to the properties of regular micro-pore structures and low-temperature process [44–48]. Vinogradov et al. first reported the TiO_2-MOF-based solar cells with an efficiency of 6.4% [49]. Utilizing the typical micro-pore structure of MOFs, Ho et al. introduced MOF-525 ($Zr_6O_4(OH)_4(TCPP\text{-}H_2)_3$) as the regular scaffold into perovskite film to mediate the arrangement of perovskite crystallites. Finally, they improved the morphology and crystallinity of the perovskite thin film [50]. Wei and coworkers used zeolitic imidazolate framework-8 as an interface layer to increase the crystallinity and grain size of perovskite film [51]. Fan et al. doped $[In_2(phen)_3Cl_6] \cdot CH_3CN \cdot 2H_2O$ into HTLs to enhance light absorption and reduce the pinholes of the film [52]. These works improved PSCs performance effectively by regulating the morphology and crystallinity of perovskite film via adding MOFs. However, to our knowledge, MOFs as dopant-free HTLs in PSCs have not been reported. In recent years, the emergence of electrically conductive MOFs provides new opportunities for their integration as electroactive components in electronic devices [53].

Herein, we firstly attempt Ni_3(2,3,6,7,10,11-hexaiminotriphenylene)$_2$ ($Ni_3(HITP)_2$) as dopant-free HTLs in PSCs to extract holes effectively for PSCs. The $Ni_3(HITP)_2$ is a p-type semiconductor material with a high hole mobility of 48.6 $cm^2 \cdot V^{-1} \cdot s^{-1}$ [54], and the $Ni_3(HITP)_2$ film can be synthesized in a low-temperature process. The thickness controllable floating film of $Ni_3(HITP)_2$ at the gas–liquid interface is transferred onto indium tin oxide (ITO)-coated glass substrate. The film possesses low surface roughness, which provides prerequisites for subsequent deposition of high-quality perovskite films. Steady-state photoluminescence (PL) spectrum shows $Ni_3(HITP)_2$ film can transport holes effectively from perovskite layer to anode. As a result, the inverted planar PSCs based on $Ni_3(HITP)_2$ film achieve the champion PCE of 10.3%.

Results and Discussion

The $Ni_3(HITP)_2$ film is transferred by the following method, and experimental details are provided in the experimental section and Additional file 1: Figure S1. After the reaction mixture is heated to 65 °C, a bluish film spontaneously spreads out and forms at the liquid–air interface because of the hydrophobic of the $Ni_3(HITP)_2$ film. Then, the ITO-coated glass substrate is placed at the air–liquid interface along the edge of the beaker in an inclined posture under the film. The side of the $Ni_3(HITP)_2$ film contact with water directly adsorbs on the ITO-coated glass substrate by homeopathically and slowly lifting. Finally, a complete $Ni_3(HITP)_2$ film is obtained. Figure 1a shows X-ray diffraction (XRD) characterization. The peaks of the XRD spectrum are located at 4.7°, 9.5°, 12.6°, 16.5°, and 27.3°. The peaks of 4.7°, 9.5°, 12.6°, and 16.5° correspond to the (100) reflections, and 27.3° originates from (001) reflection. The result is consistent with the structure of $Ni_3(HITP)_2$ reported in the previous literature [54]. The transmission electron microscope (TEM) result in Fig. 1b displays that the film is highly oriented and uniform without curling on the edges of these nanosheets. The $Ni_3(HITP)_2$ has a fringe spacing of 1.884 nm, corresponding to the (100) plane [55]. The energy-dispersive spectroscopy mapping images (Additional file 1: Figure S2) reveal the uniform element distribution of Ni, C, and N throughout the whole $Ni_3(HITP)_2$ film. X-ray photoelectron spectroscopy (XPS) (Additional file 1: Figure S3) is further carried out to identify the formation of $Ni_3(HITP)_2$ film. As shown in Fig. 1c, there are no other impurities such as NiO (853.8 eV) and $Ni(OH)_2$ (855.2 eV) in the membrane, according to the previous reports [21]. The peaks of Ni 2p are located at 873.4 eV ($2p_{1/2}$) and 855.5 eV ($2p_{3/2}$) from $Ni_3(HITP)_2$ [54]. In addition, the thermogravimetric analysis is conducted to investigate the stability of the $Ni_3(HITP)_2$ film.

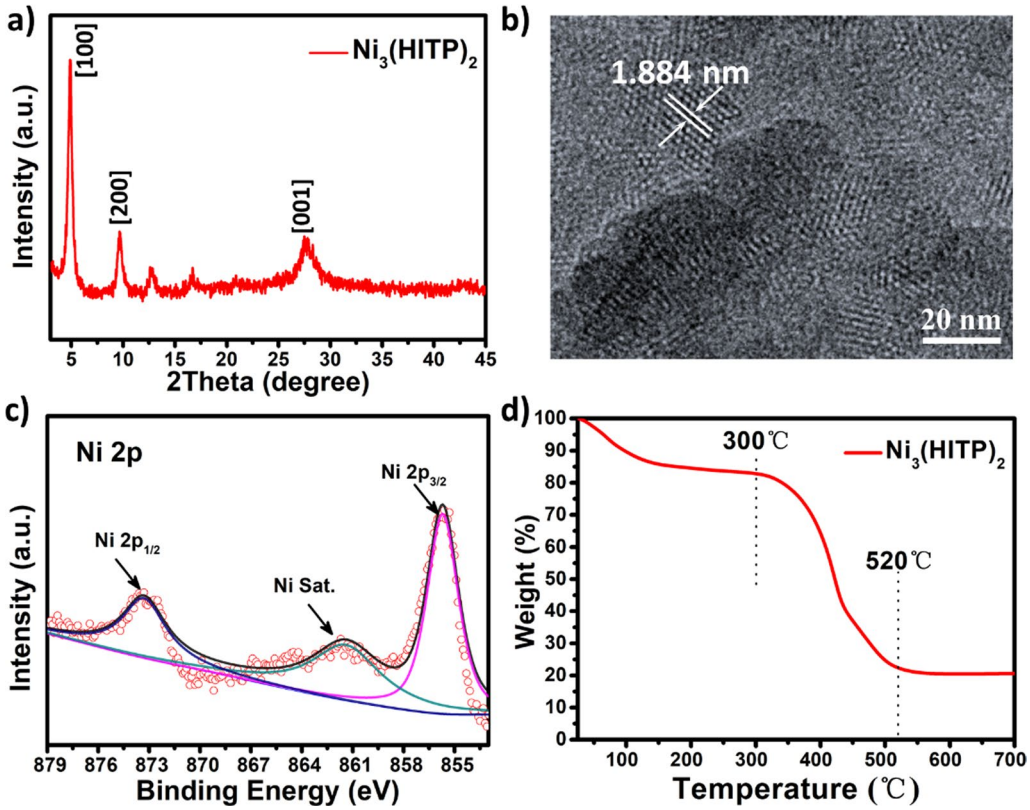

Fig. 1 Characterization of the $Ni_3(HITP)_2$ film. **a** XRD pattern, **b** TEM micrograph; **c** XPS spectra of Ni 2p, and **d** thermogravimetric curve of the $Ni_3(HITP)_2$

As can be seen from Fig. 1d, water in the film is lost at the initial stage. As the temperature increases, $Ni_3(HITP)_2$ decomposes between 300 ℃ and 520 ℃. The high thermal stability provides wider application compared with organic materials.

By controlling the reaction time, we obtained the different thickness films (Additional file 1: Figure S4). The $Ni_3(HITP)_2$ film gradually changes from light blue to bluish-black or even black as the film thickness increases (Additional file 1: Figure S5). Figure 2a shows the optical transmittance of $Ni_3(HITP)_2$ films with different thicknesses. The transmittance of these films decreases with increasing film thickness. The films with thickness of 20 and 30 nm maintain over 75% transmittance. The hole mobility of the $Ni_3(HITP)_2$ films reaches up to 48.6 $cm^2 \cdot V^{-1} \cdot s^{-1}$, and it is higher than that of most hole transport materials and even some inorganic materials. The high carrier mobility is conducive to hole transportation in photo-electronic devices [56]. The electronic properties of the $Ni_3(HITP)_2$ film are further conducted by ultraviolet photoemission spectroscopy (UPS) (Fig. 2b). The Femi level (E_f) of 4.48 eV and valence band maximum (V_B) of 4.98 eV are obtained from the secondary electron cutoff and the onset of the UPS spectra according to the following equations: $E_f = h\nu - E_{cutoff}$ and $V_B = h\nu - (E_{cutoff} - E_{onset})$, where $h\nu$ is the incident photon energy of the He (I) source (21.22 eV). Figure 2c shows the energy level alignment diagram of the inverted PSCs. The result demonstrates that the V_B of $Ni_3(HITP)_2$ and perovskite (~5.4 eV) are matched well. It indicates the $Ni_3(HITP)_2$ film is desirable to act as HTL for PSCs. Steady-state PL spectra is performed to ascertain the hole transfer ability from perovskite film to $Ni_3(HITP)_2$ layer (Fig. 2d). After introducing PEDOT/PSS, the perovskite films show strong PL quenching, indicating the holes are transferred from perovskite to HTL of PEDOT/PSS. The PL of perovskite film is further quenched, when $Ni_3(HITP)_2$ replaces PEDOT/PSS. Especially, 30 nm $Ni_3(HITP)_2$ film leads to the lowest PL intensity, suggesting more carriers are transferred effectively from perovskite to HTL. In addition, we have repeated the PL of 20 nm and 30 nm $Ni_3(HITP)_2$ for three times to compare with other thicknesses of $Ni_3(HITP)_2$ (Additional file 1: Figure S6). The graphs marked with the red box are the PL of perovskite with 20 nm and 30 nm $Ni_3(HITP)_2$ and are further amplified in the inset of Additional file 1: Figure S6. The

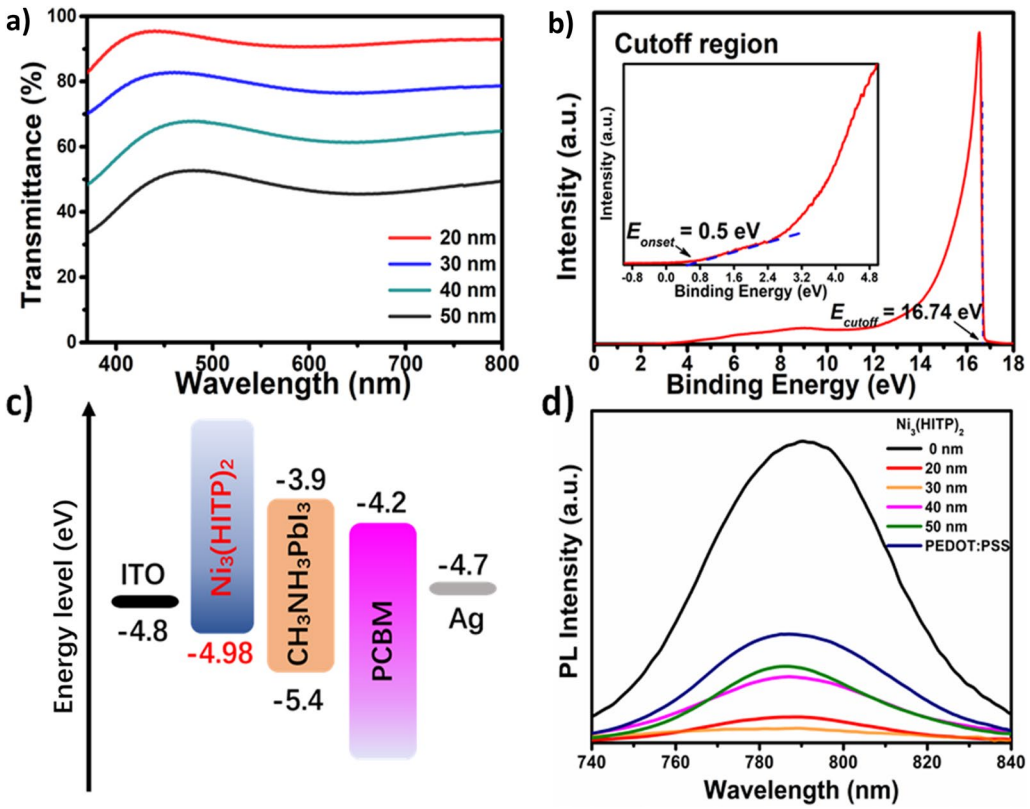

Fig. 2 Characterization of optical and electrical properties of $Ni_3(HITP)_2$ film. **a** Optical transmission spectra of different thickness of $Ni_3(HITP)_2$ films; **b** UPS spectra of $Ni_3(HITP)_2$ film; **c** Energy level alignment diagram of PSCs and **d** The steady-state PL spectra of perovskite films on different thickness $Ni_3(HITP)_2$ films

time-resolved PL measurement is carried out to analyze the hole extraction capability of $Ni_3(HITP)_2$ film (Additional file 1: Figure S7). The average decay lifetimes of the perovskite deposited on ITO substrate with different hole transport layers are listed in Additional file 1: Table S1. Compared with PEDOT/PSS, the average carriers lifetime of perovskite drops greatly upon introducing $Ni_3(HITP)_2$ film, indicating that the holes can efficiently be extracted at the interfaces of perovskite and $Ni_3(HITP)_2$. It is worthy of noting that the shorter decay lifetimes perovskite based on the 30 nm $Ni_3(HITP)_2$ film declines to 1.18 ns, revealing its high carrier extraction capability.

To investigate the surface quality of the $Ni_3(HITP)_2$ films with different thicknesses, scanning electron microscopy (SEM) images are exhibited in Fig. 3. Compared with the ITO-coated glass substrate, both 20 nm and 30 nm thickness of the $Ni_3(HITP)_2$ films remain the similar state of ITO, manifesting highly transparent property. Further increasing the thickness of films, the surface morphology character of the ITO disappears. Meanwhile, the film becomes non-uniform and has some white spots. Figure 3f and Additional file 1: Figure S8 show the surface morphology of $Ni_3(HITP)_2$ films by atomic force microscopy (AFM). The root-mean-square (RMS) roughness is 9.74 nm for the $Ni_3(HITP)_2$ films with a thickness of 20 nm. When increasing to 30 nm thickness, RMS roughness increases to 5.5 nm. Nevertheless, further increasing the thickness of $Ni_3(HITP)_2$ films, the film surface becomes rougher with RMS roughness of 14.2 nm and 16.3 nm for 40 nm and 50 nm thickness of $Ni_3(HITP)_2$ films, respectively. The results of AFM and SEM show that the $Ni_3(HITP)_2$ film with a thickness of 30 nm has a smooth and compact surface. It is the guarantee for subsequent deposition of high-quality perovskite film for solar cells.

To investigate the morphology and crystallinity of the perovskite films on $Ni_3(HITP)_2$ films, Fig. 4 and Additional file 1: Figure S9 show the surface SEM images and XRD pattern of perovskite film. The perovskite layer is prepared by a two-step method, which avoids $Ni_3(HITP)_2$ film being corroded by the solvent N, N-dimethyl formamide and dimethyl sulfoxide. As can be seen from Fig. 4, all the perovskite films based on different thicknesses of $Ni_3(HITP)_2$ films have compact surfaces, but they still have obvious differences. The grain boundary of

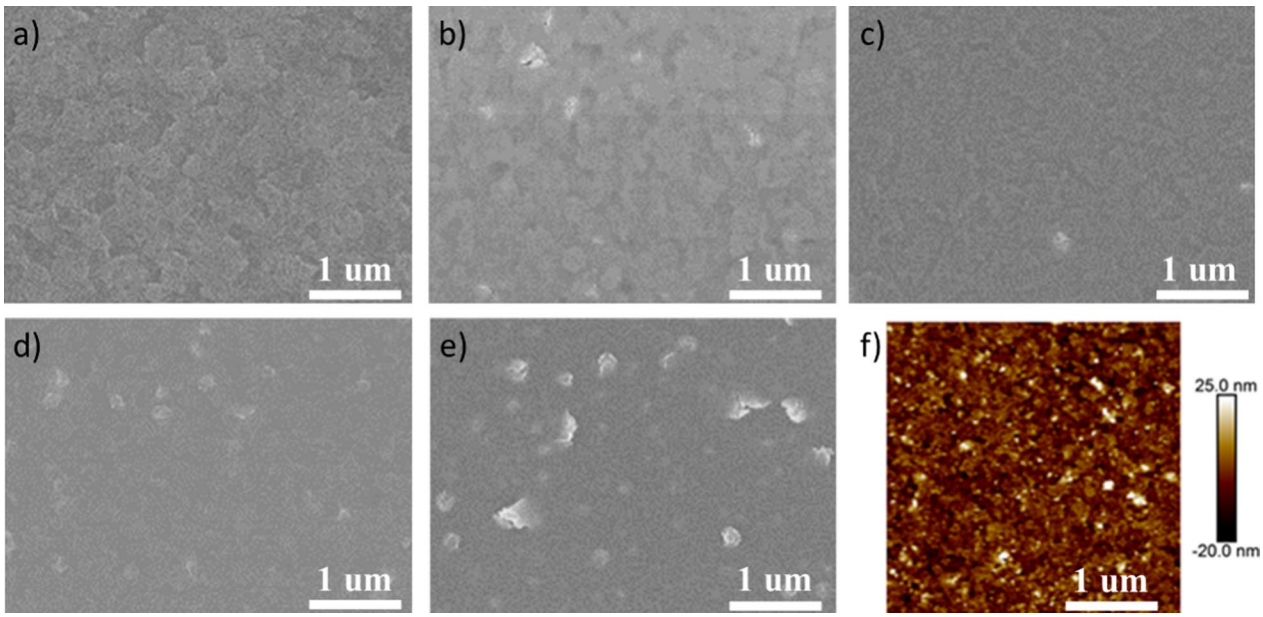

Fig. 3 Morphology characterization of $Ni_3(HITP)_2$ films with different thicknesses. SEM images of **a** Bare ITO-coated glass and **b**–**e** $Ni_3(HITP)_2$ films with 20 nm, 30 nm, 40 nm, 50 nm, respectively; **f** AFM image of $Ni_3(HITP)_2$ film of 30 nm thickness

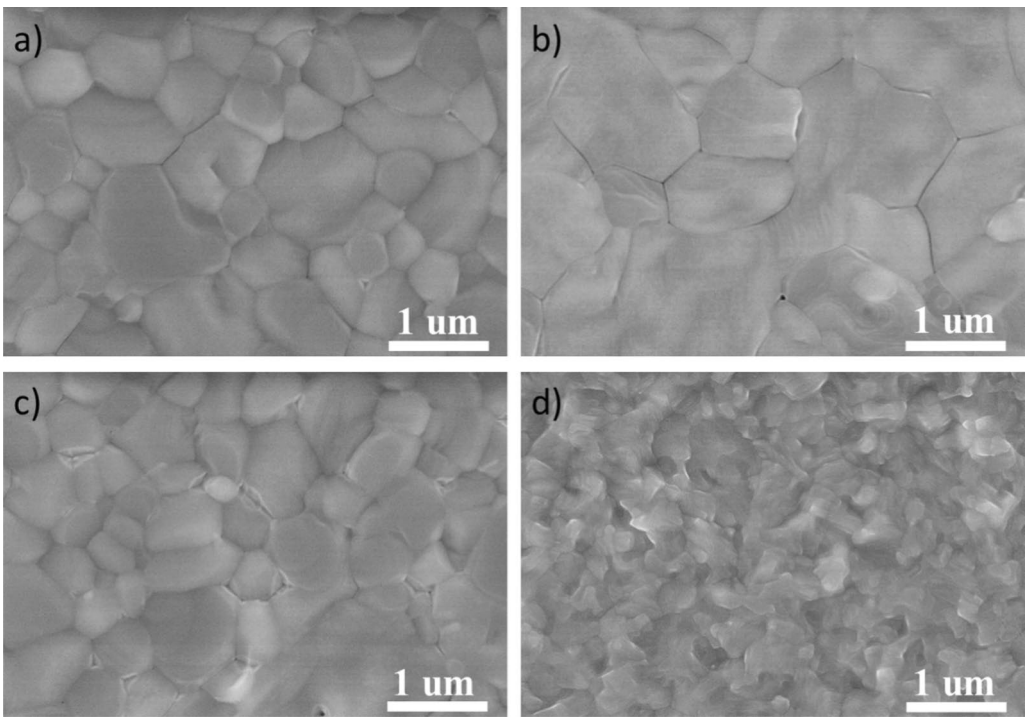

Fig. 4 Morphology characterization of perovskite films deposition on different thicknesses of $Ni_3(HITP)_2$ films. **a**–**d** 20 nm, 30 nm, 40 nm, and 50 nm, respectively

perovskite film deposited on the 20 nm $Ni_3(HITP)_2$ film is clearly visible. When increasing the thickness of the $Ni_3(HITP)_2$ film to 30 nm, the perovskite grain boundaries gradually become blurred. It indicates the perovskite grains are closely packed together. Meanwhile, the perovskite grain size is increased to 2 um, contributing to the smoother film surface of $Ni_3(HITP)_2$ film. When further increasing the thickness of $Ni_3(HITP)_2$ film, the perovskite grains become smaller, and the perovskite film surface gets uneven. Furthermore, Additional file 1: Figure S9 further shows the quality of perovskite films deposition on different thicknesses of $Ni_3(HITP)_2$ membranes. It can be seen that the XRD peak intensity of the perovskite deposited on the surface of the 30 nm-thick $Ni_3(HITP)_2$ film is higher than that of other thicknesses of perovskite films. The results demonstrate the perovskite film with 30 nm $Ni_3(HITP)_2$ has the highest crystallinity.

To build up a good performance solar cell, the $Ni_3(HITP)_2$ films with a thickness of 30 nm are used to fabricate the p-i-n type inverted PSCs due to its high transmittance, good flatness, high hole mobility, and appropriate energy level. Figure 5a shows the device has clear layers from the cross-sectional view and the thickness of perovskite is about 300 nm. The *J–V* measurement of PSCs is conducted under the standard AM 1.5G illumination. As shown in Fig. 5b, the device exhibits a negligible photocurrent hysteresis under different scanning directions [57, 58]. The champion device has a PCE of 10.3%, V_{oc} of 0.91 V, J_{sc} of 17.09 mA·cm^{-2}, and FF of 66%. Figure 5c shows the steady-state photocurrent density and efficiency evolved with time at the maximum power output point (0.75 V). A reliable output efficiency of 9.61% and photocurrent density of 15.45 mA·cm^{-2} are obtained. Figure 5d shows the external quantum efficiency (EQE) of the device. The integrated J_{sc} from

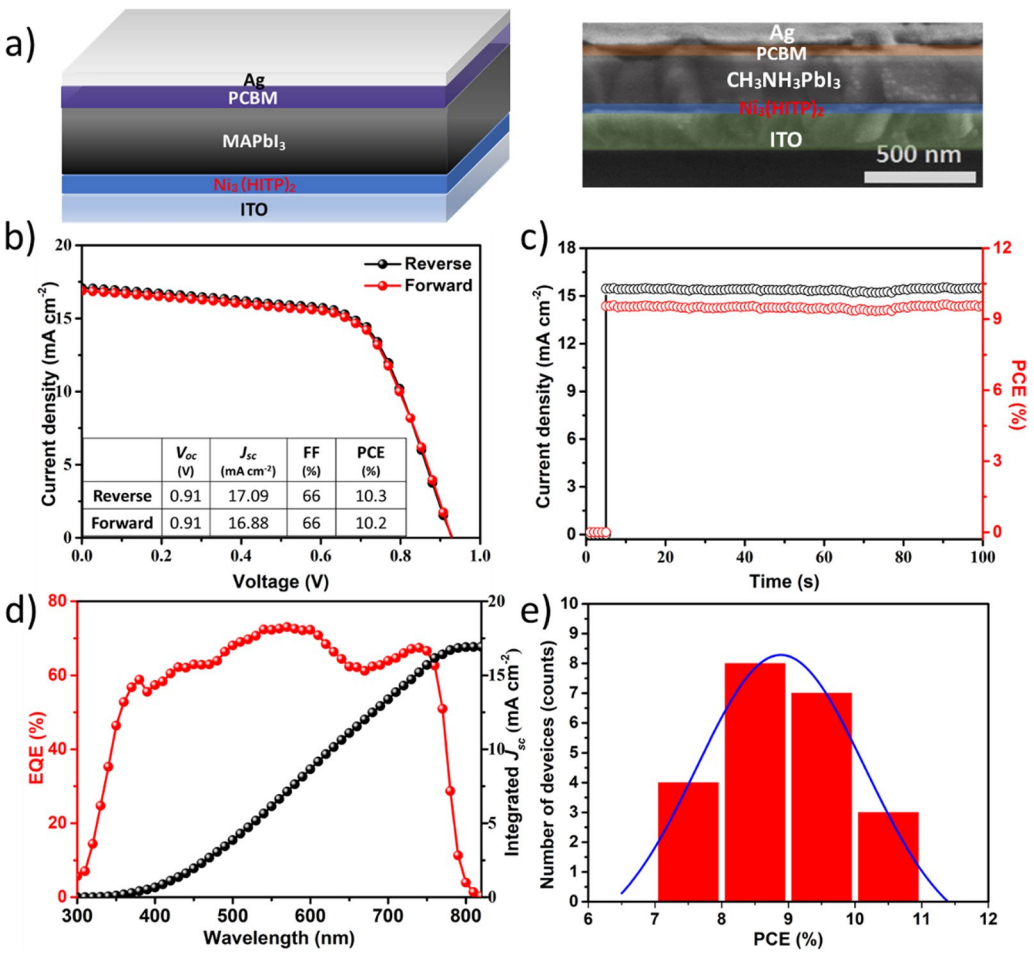

Fig. 5 The characterization of the PSCs. **a** The device structure and SEM image of cross section; **b** the *J–V* curves of the device under forward scan and reverse scan; **c** steady-state photocurrent (black curve) and output efficiency (red curve) of the device; **d** EQE and corresponding integrated J_{sc}; **e** histogram of PCEs measured from 22 PSCs

the EQE spectrum is 16.94 mA·cm^{-2}, which is consistent with the value from the *J*–*V* curve. The EQE of the device is no more than 73% at the wavelength between 400—800 nm. To overcome the problem, the $Ni_3(HITP)_2$ film is inserted between perovskite film and top electrode will be a good strategy. This kind of work is underway. In addition, Fig. 5e illustrates the good reproducibility of the devices with the PCE histogram collected from 22 independent devices.

Conclusions

In summary, a dopant-free $Ni_3(HITP)_2$ endows the suitable valence band edge and high hole mobility as HTLs for PSCs. The steady-state and time-resolved PL spectrum exhibit high hole extraction capability of $Ni_3(HITP)_2$. Inverted PSCs based on $Ni_3(HITP)_2$ films have a champion PCE of 10.3%. This work fills the gap in the application of MOFs as dopant-free hole transport layers in PSCs and expands the application field of MOFs.

Materials and Methods

Materials

All the chemicals were bought from commercial resources without additional purification. Water was purified with the Milli-Q purification system. Nickel chloride hexahydrate and ammonium hydroxide were bought from Sinopharm Chemical Reagent Co. 2,3,6,7,10,11-hexaaminotriphenylene hexahydrochloride was bought from WuXi AppTec. Lead (II) iodide was obtained from Sigma-Aldrich.

Synthesis of the $Ni_3(HITP)_2$ Film

20 mg of 2,3,6,7,10,11-hexaaminotriphenylene hexahydrochloride, 13.2 mg of nickel chloride hexahydrate, and 40.0 mL H_2O were added into a 50-mL beaker. The reaction mixture was then sonicated until the solids were completely dissolved. After that, 0.6 mL ammonium hydroxide was dropped into the beaker when the reaction mixture was heated to 65 °C. The $Ni_3(HITP)_2$ film was formed at the air–liquid interface after 1 min. Different thickness of the films was controlled by the reaction time.

Device Fabrication

ITO-coated glass substrates were sequentially cleaned by sonication with acetone, deionized water, and ethyl alcohol and then were treated using UV-ozone. The processed ITO glass was extended to the bottom of the film along the edge of the beaker in an inclined posture. The complete $Ni_3(HITP)_2$ film was obtained by homeopathically and slowly lifted onto ITO-coated glass substrate. Then, after further cleaning and drying the $Ni_3(HITP)_2$ film adsorbed on ITO-coated glass substrate, the perovskite layer was fabricated as described in our previous report [57]. The electron-transporting layer, $PC_{61}BM$ (methyl [6, 6]-phenyl-C_{61}-butyrate) (20 mg/mL in chlorobenzene) was deposited by spin-coating. Finally, the Ag electrode was thermally evaporated in a high vacuum chamber through a metal mask. The device's effective area was 0.0725 cm^2.

Characterization

The morphologies images were obtained using AFM (Bruker) and SEM (Hitachi SU8010). The TEM images were obtained by using FEI Tecnai F-20 microscope equipped with a field-emission gun (operating at 200 kV). The transmission spectra of the films were recorded by the Shimadzu spectrophotometer (mode UV2450) for PL measurements were performed by a Horiba spectrofluorometer (Fluoromax-4). The wavelength of the excitation light source is 525 nm. XRD and TGA measurements were carried out on the D8 Advance (Bruker) and TG/DTG7300 (SII NanoTechnology), respectively. XPS and UPS were performed by the Escalab 250Xi (Thermo Fisher). The *J*–*V* characteristics of devices were recorded from a programmable Keithley 2400 source meter under simulated AM 1.5G solar irradiation at 100 mW·cm^{-2} in air condition.

Abbreviations

PSCs: Perovskite solar cells; PCE: Power conversion efficiency; ITO: Indium tin oxide; HTLs: Hole transport layers; Spiro-OMeTAD: 2,2′,7,7′-Tetrakis(*N*,*N*′-di-*p*-methoxyphenylamine)-9,9′-spirobiflurorene; MOFs: Metal–organic frameworks; $Ni_3(HITP)_2$: Ni_3(2,3,6,7,10,11-hexaiminotriphenylene)$_2$; PL: Steady-state photoluminescence; EQE: External quantum efficiency; XRD: X-ray diffraction; TEM: Transmission electron microscope; XPS: X-ray photoelectron spectroscopy; UPS: Ultraviolet photoemission spectroscopy; E_f: Femi level; V_B: Valence band maximum; SEM: Scanning electron microscopy; AFM: Atomic force microscopy; RMS: Root-mean-square.

Supplementary Information

The online version contains supplementary material available at https://doi.org/10.1186/s11671-021-03643-7.

Additional file 1: Figure S1. Illustration of the assembly process for the $Ni_3(HITP)_2$ film. **Figure S2**. EDX mapping of the $Ni_3(HITP)_2$ membranes. **Figure S3**. XPS spectra of the $Ni_3(HITP)_2$ membranes. **Figure S4**. AFM images of different thicknesses of $Ni_3(HITP)_2$ membranes. **Figure S5**. Photographs of the bare ITO glass and with different thicknesses of $Ni_3(HITP)_2$ membranes. **Figure S6**. Steady-state PL spectra of perovskite/ITO based on 20 nm, 30 nm, 40 nm, and 50 nm $Ni_3(HITP)_2$ film and PEDOT/PSS; Inset: the enlarged steady-state PL spectra of perovskite on the 20 nm and 30 nm $Ni_3(HITP)_2$ film repeated by three times, respectively. **Figure S7**. Time-resolved PL spectra of perovskite on the ITO substrate with different thicknesses of $Ni_3(HITP)_2$ film and PEDOT/PSS. **Figure S8**. AFM images of different thicknesses of $Ni_3(HITP)_2$ membranes. **Figure S9**. XRD pattern of perovskite films deposition on different thicknesses of $Ni_3(HITP)_2$ membranes. **Table S1**. The average decay lifetimes of the perovskite/ITO with different hole transport layers.

Acknowledgements
We gratefully acknowledge the support from the Priority Academic Program Development (PADA) of Jiangsu Higher Education Institutions for Optical Engineering, the Key Lab of Advanced Optical Manufacturing Technologies of Jiangsu Province and Key Lab of Modern Optical Technologies of Education Ministry of China in Soochow University, and Jiangsu Collaborative Innovation Center of Photovoltaic Science and Engineering in Changzhou University.

Authors' contributions
GZ and YL conceived the research project. CS completed the synthesis of the MOFs materials under the supervision of GX. CS, RW, and WY performed the experiments of the devices and wrote the paper under the supervision of GZ and YL. KC, SD, JW, FY, and CP provided valuable discussion. All authors read and approved the final manuscript.

Funding
Not applicable.

Availability of data and materials
All data supporting the conclusions of this article are included within the article and supplementary document.

Declarations

Competing interests
The authors declare no competing interests.

Author details
[1]College of Energy, Soochow Institute for Energy and Materials Innovations, and Key Laboratory of Advanced Carbon Materials and Wearable Energy Technologies of Jiangsu Province, Soochow University, Suzhou 215123, People's Republic of China. [2]School of Resources Environmental and Chemical Engineering, Nanchang University, 999 Xuefu Avenue, Nanchang 330031, China. [3]State Key Laboratory of Structural Chemistry, Fujian Institute of Research on the Structure of Matter, Chinese Academy of Sciences, Fuzhou 350002, Fujian, China. [4]School for Engineering of Matter, Transport and Energy, Arizona State University, 551 E. Tyler Mall, Tempe, AZ 85287, USA. [5]Institute of Fundamental and Frontier Sciences, University of Electronic Science and Technology of China, Chengdu 610054, People's Republic of China. [6]College of Chemistry, Chemical Engineering and Materials Science, Soochow Universit, Suzhou 215123, People's Republic of China. [7]School of Optoelectronic Science and Engineering and Collaborative Innovation Center of Suzhou Nano Science and Technology, Soochow University, Suzhou 215006, People's Republic of China.

Received: 14 August 2021 Accepted: 19 December 2021
Published online: 04 January 2022

References

1. Zheng X, Hou Y, Bao C, Yin J, Yuan F, Huang Z et al (2020) Managing grains and interfaces via ligand anchoring enables 22.3%-efficiency inverted perovskite solar cells. Nat Energy 5:131–140
2. Jung EH, Jeon NJ, Park EY, Moon CS, Shin TJ, Yang TY et al (2019) Efficient, stable and scalable perovskite solar cells using poly(3-hexylthiophene). Nature 567:511–515
3. Bai S, Da P, Li C, Wang Z, Yuan Z, Fu F et al (2019) Planar perovskite solar cells with long-term stability using ionic liquid additives. Nature 571:245–250
4. Zhao D, Yu Y, Wang C, Liao W, Shrestha N, Grice CR et al (2017) Low-bandgap mixed tin–lead iodide perovskite absorbers with long carrier lifetimes for all-perovskite tandem solar cells. Nat Energy 2:17018
5. Xu XL, Xiao LB, Zhao J, Pan BK, Li J, Liao WQ et al (2020) Molecular ferroelectrics-driven high-performance perovskite solar cells. Angew Chem Int Ed Engl 59:19974–19982
6. Chen Y, Yang Z, Wang S, Zheng X, Wu Y, Yuan N et al (2018) Design of an inorganic mesoporous hole-transporting layer for highly efficient and stable inverted perovskite solar cells. Adv Mater 30:1805660
7. Wang Y, Wu T, Barbaud J, Kong W, Cui D, Chen H et al (2019) Stabilizing heterostructures of soft perovskite semiconductors. Sci 365:687–691
8. Wu R, Yao J, Wang S, Zhou X, Wang Q, Gao L et al (2019) Ultracompact, well-packed perovskite flat crystals: preparation and application in planar solar cells with high efficiency and humidity tolerance. ACS Appl Mater Interfaces 11:11283–11291
9. Huang L, Zhou X, Xue R, Xu P, Wang S, Xu C et al (2020) Low-temperature growing anatase TiO_2/SnO_2 multi-dimensional heterojunctions at MXene conductive network for high-efficient perovskite solar cells. Nanomicro Lett 12:44
10. NREL, best research-cell efficiencies chart. https://www.nrel.gov/pv/cell-efficiency.html . Accessed Sept 2020
11. Liu M, Johnston MB, Snaith HJ (2013) Efficient planar heterojunction perovskite solar cells by vapour deposition. Nature 501:395–398
12. Haitao X, Feng Y, Dan Z, Xunfan L, Lie C, Yiwang C (2020) Hole transport layers for organic solar cells: recent progress and prospects. J Mater Chem A 8:11478–11492
13. Wu T, Wang Z, Xiao L, Qin P, Qin Z, Ma L et al (2021) Mesoporous Au@Cu2−xS core-shell nanoparticles with double localized surface plasmon resonance and ligand modulation for hole-selective passivation in perovskite solar cells. Sol RRL 5:2100358
14. Zheng Y, Ge B, Zheng LR, Hou Y, Yang S, Yang HG (2021) Solution-processable nickel–chromium ternary oxide as an efficient hole transport layer for inverted planar perovskite solar cells. J Mater Chem A 9:21792–21798
15. Du Q, Shen Z, Chen C, Li F, Jin M, Li H et al (2021) Spiro-OMeTAD:Sb2S3 hole transport layer with triple functions of overcoming lithium salt aggregation, long-term high conductivity, and defect passivation for perovskite solar cells. Sol RRL 5:2100622
16. Wang Z-K, Liao L-S (2018) Doped charge-transporting layers in planar perovskite solar cells. Adv Opt Mater 6:1800276
17. Pham HD, Yang TCJ, Jain SM, Wilson GJ, Sonar P (2020) Development of dopant-free organic hole transporting materials for perovskite solar cells. Adv Energy Mater 10:1903326
18. Ma Z, Xiao Z, Liu Q, Huang D, Zhou W, Jiang H et al (2020) Oxidization-free spiro-OMeTAD hole-transporting layer for efficient CsPbI2Br perovskite solar cells. ACS Appl Mater Interfaces 12:52779–52787
19. Reza KM, Gurung A, Bahrami B, Mabrouk S, Elbohy H, Pathak R et al (2020) Tailored PEDOT:PSS hole transport layer for higher performance in perovskite solar cells: enhancement of electrical and optical properties with improved morphology. J Energy Chem 44:41–50
20. Xu C, Liu Z, Lee E-C (2018) High-performance metal oxide-free inverted perovskite solar cells using poly(bis(4-phenyl)(2,4,6-trimethylphenyl) amine) as the hole transport layer. J Mater Chem C 6:6975–6981
21. Wang X, Wu J, Yang Y, Liu X, Guo Q, Song Z et al (2019) High performance and stable perovskite solar cells using vanadic oxide as a dopant for spiro-OMeTAD. J Mater Chem A 7:13256–13264
22. Cong S, Yang H, Lou Y, Han L, Yi Q, Wang H et al (2017) Organic small molecule as the underlayer toward high performance planar perovskite solar cells. ACS Appl Mater Interfaces 9:2295–2300
23. Ryu S, Noh JH, Jeon NJ, Chan Kim Y, Yang WS, Seo J et al (2014) Voltage output of efficient perovskite solar cells with high open-circuit voltage and fill factor. Energy Environ Sci 7:2614–2618
24. Stranks SD, Snaith HJ (2015) Metal-halide perovskites for photovoltaic and light-emitting devices. Nat Nanotechnol 10:391–402
25. Lu H, Ma Y, Gu B, Tian W, Li L (2015) Identifying the optimum thickness of electron transport layers for highly efficient perovskite planar solar cells. J Mater Chem A 3:16445–16452
26. Wang Y, Yue Y, Yang X, Han L (2018) Toward long-term stable and highly efficient perovskite solar cells via effective charge transporting materials. Adv Energy Mater 8:1800249
27. Urieta-Mora J, Garcia-Benito I, Molina-Ontoria A, Martin N (2018) Hole transporting materials for perovskite solar cells: a chemical approach. Chem Soc Rev 47:8541–8571
28. Lamberti F, Gatti T, Cescon E, Sorrentino R, Rizzo A, Menna E et al (2019) Evidence of Spiro-OMeTAD de-doping by tert-butylpyridine additive in hole-transporting layers for perovskite solar cells. Chem 5:1806–1817
29. Zhang L, Jiang C, Wu C, Ju H, Jiang G, Liu W et al (2018) V2O5 as hole transporting material for efficient all inorganic Sb2S3 solar cells. ACS Appl Mater Interfaces 10:27098–27105
30. Zuo C, Ding L (2015) Solution-processed Cu_2O and CuO as hole transport materials for efficient perovskite solar cells. Small 11:5528–5532

31. Schulz P, Tiepelt JO, Christians JA, Levine I, Edri E, Sanehira EM et al (2016) High-work-function molybdenum oxide hole extraction contacts in hybrid organic-inorganic perovskite solar cells. ACS Appl Mater Interfaces 8:31491–31499
32. Ye S, Sun W, Li Y, Yan W, Peng H, Bian Z et al (2015) CuSCN-based inverted planar perovskite solar cell with an average PCE of 15.6%. Nano Lett 15:3723–3728
33. You J, Meng L, Song TB, Guo TF, Yang YM, Chang WH et al (2016) Improved air stability of perovskite solar cells via solution-processed metal oxide transport layers. Nat Nanotechnol 11:75–81
34. Fakharuddin A, Vasilopoulou M, Soultati A, Haider MI, Briscoe J, Fotopoulos V et al (2021) Robust inorganic hole transport materials for organic and perovskite solar cells: insights into materials electronic properties and device performance. Sol RRL 5:2000555
35. Yang X, Lin X, Zhao YS, Yan D (2018) Recent advances in micro-/nanostructured metal–organic frameworks towards photonic and electronic applications. Chemistry 24:6484–6493
36. Da-Wei F, Wen Z, Hong-Ling C, Yi Z, Jia-Zhen G, Ren-Gen X et al (2011) A multiferroic perdeutero metal–organic framework†. Angew Chem 123:12153–12157
37. Shah BB, Kundu T, Zhao D (2019) Mechanical properties of shaped metal–organic frameworks. Top Curr Chem (Cham) 377(5):25
38. Xu Y, Li Q, Xue H, Pang H (2018) Metal–organic frameworks for direct electrochemical applications. Coord Chem Rev 376:292–318
39. Usman M, Mendiratta S, Lu KL (2017) Semiconductor metal–organic frameworks: future low-bandgap materials. Adv Mater 29:1605071
40. Huang T, Lou Z, Lu Y, Li R, Jiang Y, Shen G et al (2019) Metal–organic-framework-derived MCo_2O_4 (M═Mn and Zn) nanosheet arrays on carbon cloth as integrated anodes for energy storage applications. ChemElectroChem 6:5836–5843
41. Allendorf MD, Dong R, Feng X, Kaskel S, Matoga D, Stavila V (2020) Electronic devices using open framework materials. Chem Rev 120:8581–8640
42. Allendorf MD, Schwartzberg A, Stavila V, Talin AA (2011) A roadmap to implementing metal–organic frameworks in electronic devices: challenges and critical directions. Chemistry 17:11372–11388
43. Tong P, Liang J, Jiang X, Li J (2020) Research progress on metal–organic framework composites in chemical sensors. Crit Rev Anal Chem 50:376–392
44. Furukawa H, Cordova KE, O'Keeffe M, Yaghi OM (2013) The chemistry and applications of metal–organic frameworks. Sci 341:1230444
45. Ferey G (2008) Hybrid porous solids: past, present, future. Chem Soc Rev 37:191–214
46. Shen M, Zhang Y, Xu H, Ma H (2021) MOFs based on the application and challenges of perovskite solar cells. iScience 24:103069
47. Heo DY, Do HH, Ahn SH, Kim SY (2020) Metal–organic framework materials for perovskite solar cells. Polymers (Basel) 12:2061
48. Huang L, Zhou X, Wu R, Shi C, Xue R, Zou J et al (2019) Oriented haloing metal–organic framework providing high efficiency and high moisture-resistance for perovskite solar cells. J Power Sources 433:226699
49. Vinogradov AV, Zaake-Hertling H, Hey-Hawkins E, Agafonov AV, Seisenbaeva GA, Kessler VG et al (2014) The first depleted heterojunction TiO_2-MOF-based solar cell. Chem Commun (Camb) 50:10210–10213
50. Chang TH, Kung CW, Chen HW, Huang TY, Kao SY, Lu HC et al (2015) Planar heterojunction perovskite solar cells incorporating metal–organic framework nanocrystals. Adv Mater 27:7229–7235
51. Shen D, Pang A, Li Y, Dou J, Wei M (2018) Metal–organic frameworks at interfaces of hybrid perovskite solar cells for enhanced photovoltaic properties. Chem Commun (Camb) 54:1253–1256
52. Li M, Xia D, Yang Y, Du X, Dong G, Jiang A et al (2018) Doping of In-2(phen)(3)Cl-6 center dot CH3CN center dot 2H(2)O indium-based metal–organic framework into hole transport layer for enhancing perovskite solar cell efficiencies. Adv Energy Mater 8:1702052
53. Ryu U, Jee S, Park JS, Han IK, Lee JH, Park M et al (2018) Nanocrystalline titanium metal–organic frameworks for highly efficient and flexible perovskite solar cells. ACS Nano 12:4968–4975
54. Wu G, Huang J, Zang Y, He J, Xu G (2017) Porous field-effect transistors based on a semiconductive metal–organic framework. J Am Chem Soc 139:1360–1363
55. Sun L, Liao B, Sheberla D, Kraemer D, Zhou J, Stach EA et al (2017) A microporous and naturally nanostructured thermoelectric metal–organic framework with ultralow thermal conductivity. Joule 1:168–177
56. Kim G-W, Lee J, Kang G, Kim T, Park T (2018) Donor-acceptor type dopant-free, polymeric hole transport material for planar perovskite solar cells (19.8%). Adv Energy Mater 8:1701935
57. Han L, Cong S, Yang H, Lou Y, Wang H, Huang J et al (2018) Environmental-friendly urea additive induced large perovskite grains for high performance inverted solar cells. Sol RRL 2:1800054
58. Shang R, Zhou Z, Nishioka H, Halim H, Furukawa S, Takei I et al (2018) Disodium benzodipyrrole sulfonate as neutral hole-transporting materials for perovskite solar cells. J Am Chem Soc 140:5018–5022

Publisher's Note